All-Optical PAM4 to 16QAM Modulation Format Conversion Using Nonlinear Optical Loop Mirror and 1:2 Coupler

Yuta MATSUMOTO[†], *Student Member*, **Ken MISHINA**[†a)], **Daisuke HISANO**[†], *Members*, *and* **Akihiro MARUTA**[†], *Senior Member*

SUMMARY   In inter-data center networks where high transmission capacity and spectral efficiency are required, a 16QAM format is deployed. On the other hand, in intra-data center networks, a PAM4 format is deployed to meet the demand for a simple and low-cost transceiver configuration. For a seamless and effective connection of such heterogeneous networks without using optical–electrical–optical conversion, an all-optical modulation format conversion technique is required. In this paper, we propose an all-optical PAM4 to 16QAM modulation format conversion using nonlinear optical loop mirror. The successful conversion operation from 2 × 26.6-Gbaud PAM4 signals to a 100-Gbps class 16QAM signal is verified by numerical simulation. Compared with an ideal 16QAM signal, the power penalty of the converted 16QAM signal can be kept within 0.51 dB.
key words: *all-optical signal processing, modulation format conversion, nonlinear optical effect, NOLM, PAM4, 16QAM*

1. Introduction

Internet traffic has vastly increased in recent years. It is anticipated that it will continue to increase because of the appearance of innovative large-capacity services based on 5G systems and IoT [1]. To meet the demand of the increasing Internet traffic, multi-level modulation formats have been widely deployed for high-capacity and high-spectral efficiency transmission in optical fiber communication networks. In inter-data center networks, 100 or 400-Gbps transmission systems, which employ quadrature-phase-shift-keying (QPSK) and 16 quadrature amplitude modulation (QAM) formats using digital coherent technology, have been implemented [2], [3]. On the other hand, in intra-data center networks, a four-level pulse amplitude modulation (PAM4) format, which is one of the multi-level modulation formats using a cost-effective intensity modulation/direct detection (IM/DD) transceiver, is expected to serve as the main modulation format [4]. As shown in Fig. 1, a modulation format conversion between PAM4 and QPSK or 16QAM is required at gateway nodes connecting different data centers. In addition, a wavelength conversion is necessary because O- and C-bands are respectively used in intra- and inter-data center networks.

Moreover, it is essential to develop signal processing technologies for network nodes that is capable of supporting
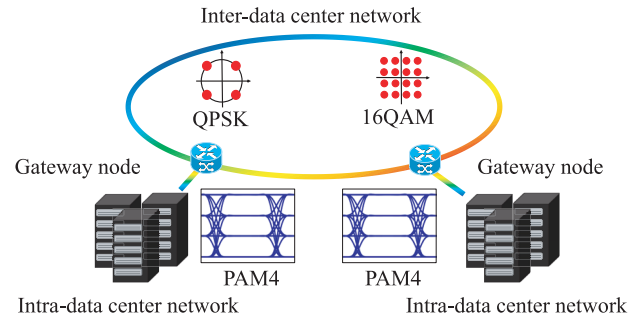
Fig. 1   A network connecting data centers.

advanced transmission technologies. All-optical signal processing is a promising technology for the realization of flexible and power-efficient all-optical photonic networks [5]. There are some advantages when considering signal processing in the optical domain. The first one is the avoidance of inefficient optical-to-electrical-to-optical conversion. The second is reduction of latency caused in electronic processing chips. These chips serve as channel de-multiplexers and may introduce extra time delay. In other words, an all-optical approach is suitable for new services requiring ultra-low latency.

A number of studies have been carried out on all-optical modulation format conversion using various optical devices [6]–[20] as summarized in Table 1. Initially, OOK to PSK format conversions using semiconductor optical amplifiers and highly nonlinear fibers (HNLF) were demonstrated [7], [8]. Recently, several studies on all-optical modulation format conversions for multi-level modulation format, such as OOK to 16QAM [10] and PAM4 to QPSK [11] have been reported. The connection of data center networks requires format conversions to meet the demand for high-capacity transmission between data centers. However, no studies on all-optical modulation format conversion from PAM4 to 16QAM have been reported in the literature.

All-optical wavelength converter is another important technology to realize all-optical photonic networks. Optical wavelength conversion can be done using various nonlinear materials and devices including HNLF [21], semiconductor optical amplifier [22], silicon (Si) waveguides [23], periodically poled lithium niobate (PPLN) [24], and so on. Ultra-wideband wavelength conversions have been also reported, such as 744-nm wavelength conversion from 1999.65 to 1255.35 nm using an AlGaAsOI nanowaveguide [25], cas-

Table 1 Summary of previous researchs on all-optical format conversion (⋆: this work).

		After modulation format conversion (MFC)				
		OOK	PAM4	BPSK	QPSK	16QAM
Before MFC	OOK	—		[7], [8]	[9]	[10]
	PAM4		—		[11]	⋆
	BPSK	[12]		—	[13]	[14]
	QPSK		[15]	[16], [17]	—	[18]
	16QAM		[19]		[20]	—

caded wavelength conversion from 1546.8 to 1312 nm based on Si waveguides [26], 1400–1600 nm wavelength conversion using PPLN [27]. It is expected to realize all-optical photonic nodes connecting data centers by combining all-optical modulation format converters with wavelength converters.

    In this paper, we propose a novel all-optical modulation format conversion from PAM4 to 16QAM using nonlinear optical loop mirror (NOLM) and a 1 : 2 coupler. The well-defined constellation diagram of the converted 100-Gbps class 16QAM signal is demonstrated by numerical simulation which indicates the feasibility of the proposed converter for high-speed operation. A power penalty of 0.51 dB of the converted 16QAM signal compared with an ideal 16QAM signal is presented. Then, the format conversion performance when the wavelength, power and timing of the input PAM4 signal are changed is discussed. In addition, we investigate influences of the waveform distortion of PAM4 signal due to amplified spontaneous emission (ASE) noise and chromatic dispersion.

2. Principle of Operation

Figure 2 shows the configuration of the proposed all-optical PAM4 to 16QAM converter. We employ the effect of cross-phase modulation (XPM) in HNLF for the modulation format conversion. As shown in Fig. 2, the converter mainly consists of the NOLM and a 1 : 2 optical coupler (OC) [10]. The converter's ports are tagged as ports 1, 2, 3, and 4. The 1 : 2 OC has a 1 : 2 power-splitting ratio and the phases of the coupled output signal and the through output signal are 90° apart. Port 3 is the input port of this converter.

    Continuous wave (CW) light is launched in port 3 as a probe light, and then, it is split by the 1 : 2 optical coupler with a 1 : 2 power ratio. The complex envelope amplitude of the electric field of the probe light launched in port 3 is defined as E_{in}. The complex envelope amplitudes E_c and E_{cc} of the probe light electric field, which splits into port 1 and 2, are respectively described as

$$E_c = \sqrt{\frac{1}{3}} E_{in}, \qquad (1)$$

$$E_{cc} = i\sqrt{\frac{2}{3}} E_{in}. \qquad (2)$$

The probe light launched in port 1 is coupled with PAM4 signal 1 by a 1 : 1 OC and propagates clockwise through the NOLM. The phase of the probe light is modulated according
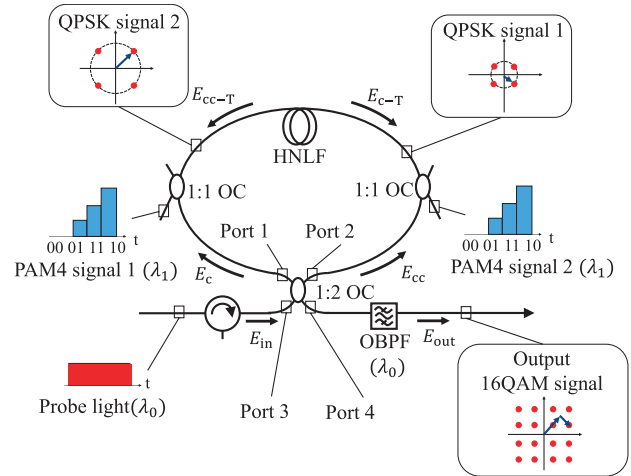

Fig. 2 Configuration of the proposed PAM4 to 16QAM converter.

to the power of PAM4 signal 1 by XPM in the HNLF. The amount of phase change $\phi_c^{(j)}$ of the clockwise probe light by the XPM is described as

$$\phi_c^{(j)} = 2\gamma L_{eff} P_c^{(j)} \ (j = 0, 1, 2, 3), \qquad (3)$$

where L_{eff} and γ are the effective length and the nonlinear coefficient of the HNLF, respectively. L_{eff} is defined by

$$L_{eff} = \frac{1 - \exp(-\alpha L)}{\alpha}, \qquad (4)$$

where α and L are the attenuation constant and the length of the HNLF, respectively. $P_c^{(j)}$ is the peak power of PAM4 signal 1, and the subscript j represents each information sequence in PAM4 signal 1. The peak power $P_c^{(j)}$ ($j = 0, 1, 2, 3$) is properly adjusted so that the phase change of the clockwise probe light $\phi_c^{(j)}$ is 0, $\pi/2$, π, and $3\pi/2$. Then, the converted QPSK signal 1 is obtained at the output of the HNLF [11]. In the same way, the probe light propagating counter-clockwise is coupled with PAM4 signal 2 and converted to QPSK signal 2. The amount of phase change $\phi_{cc}^{(k)}$ of the counter-clockwise probe light by the XPM is represented as

$$\phi_{cc}^{(k)} = 2\gamma L_{eff} P_{cc}^{(k)} \ (k = 0, 1, 2, 3), \qquad (5)$$

where $P_{cc}^{(k)}$ denotes the peak powers of PAM4 signal 2, and the subscript k represents each information sequence in PAM4 signal 2. The complex envelope amplitudes $E_{c-T}^{(j)}$ and $E_{cc-T}^{(k)}$ of the electric field at the HNLF output of the probe light propagating clockwise and counter-clockwise are

$$E_{c-T}^{(j)} = \exp\left(i\phi_c^{(j)}\right) E_c = \sqrt{\frac{1}{3}} \exp\left(i\phi_c^{(j)}\right) E_{in}, \qquad (6)$$

$$E_{cc-T}^{(k)} = \exp\left(i\phi_{cc}^{(k)}\right) E_{cc} = i\sqrt{\frac{2}{3}} \exp\left(i\phi_{cc}^{(k)}\right) E_{in}. \qquad (7)$$

Subsequently, the converted QPSK signals 1 and 2 are coupled by the 1 : 2 OC. Then, the converted 16QAM signal

can be obtained by extracting only the probe light component using an optical band-pass filter (OBPF) at port 4. The complex envelope amplitude $E_{\text{out}}^{(j,k)}$ of the electric field at the output of converter is described as

$$
\begin{aligned}
E_{\text{out}}^{(j,k)} &= \sqrt{\frac{1}{3}} E_{\text{c-T}}^{(j)} + i\sqrt{\frac{2}{3}} E_{\text{cc-T}}^{(k)} \\
&= \frac{1}{3}\left\{ \exp\left(i\phi_{\text{c}}^{(j)}\right) - 2\exp\left(i\phi_{\text{cc}}^{(k)}\right)\right\} E_{\text{in}}. \quad (8)
\end{aligned}
$$

3. Numerical Simulation

3.1 Basic Operation

We verified the operation of the proposed converter by performing a numerical simulation of the all-optical PAM4 to 16QAM conversion. Figure 3 shows the simulation model of the proposed modulation format conversion. Assuming that the interference between the clockwise and counter-clockwise lights in the NOLM is negligible, we transformed the simulation model from a Sagnac interferometer model into a Mach-Zehnder interferometer (MZI) model to simplify the simulation [10]. The upper arm of the MZI configuration corresponds to the clockwise propagation in the NOLM, and the lower arm is the counter-clockwise propagation. We used the identical HNLFs both in the upper and lower arms of the MZI. In this simulation, we calculated the electric fields of the probe light at the outputs of
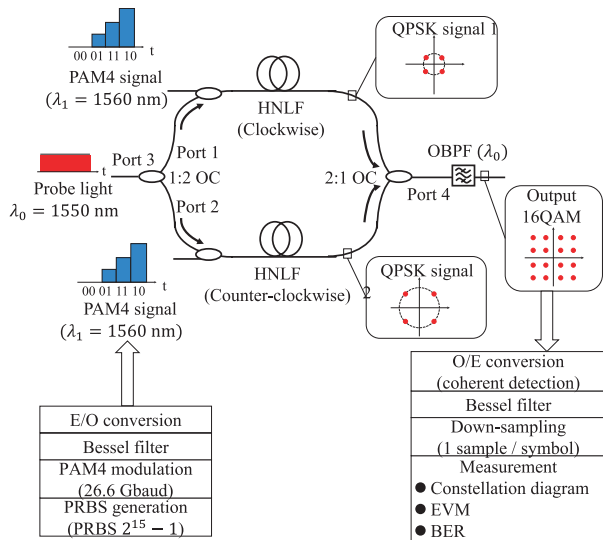
the HNLF and the converter. The complex envelope amplitude $E(z,t)[\sqrt{\text{W}}]$ of the electric field propagating in the HNLF is described by the following nonlinear Schrödinger equation (NLSE) [28]

$$
i\frac{\partial E}{\partial z} - \frac{\beta_2}{2}\frac{\partial^2 E}{\partial t^2} + \gamma|E|^2 E = -\frac{i\alpha}{2}E + i\frac{\beta_3}{6}\frac{\partial^3 E}{\partial t^3}, \quad (9)
$$

where z [m] is the propagation distance, t [s] is the time measured for reference frame moving with the group velocity, β_2 [s²/m] is the group velocity dispersion (GVD) coefficient, γ [1/(m·W)] is the nonlinear coefficient, α [1/m] is the loss coefficient, and β_3[s³/m] is the third-order dispersion coefficient. We numerically solve the NLSE by using the split-step Fourier method. The parameters of the HNLF are summarized in Table 2. 26.6-Gbaud PAM4 signals were generated as input signals using a pseudo-random bit sequence (PRBS) of length $2^{15}-1$. The wavelengths of the two PAM4 signals and the probe light were 1560 and 1550 nm, respectively. The power levels of the PAM4 signals were 0, 28, 55, and 83 mW for the four signal levels. At the output of the converter, we measured constellation diagram, error vector magnitude (EVM), and bit error rate (BER) after demodulation.

The eye diagram of the input PAM4 signal is shown in Fig. 4(a). Figure 4(b) and (c) show the constellation diagrams of the QPSK signals 1 and 2 at the outputs of the HNLF, respectively. Figure 4(d) shows the constellation diagrams of the 16QAM signal at the output of the converter. In Fig. 4(b)–(d), the black lines represent the transition of the amplitude and phase of the probe light on the I/Q plane, and the red dots represent the constellation diagram after down-sampling. It is observed that the phases of the probe lights are changed depending on the four peak powers of the PAM4 signals, and that two QPSK signals are generated. After coupling the two QPSK signals by the 1 : 2 coupler, a well-defined constellation diagram of a converted 100-Gbps
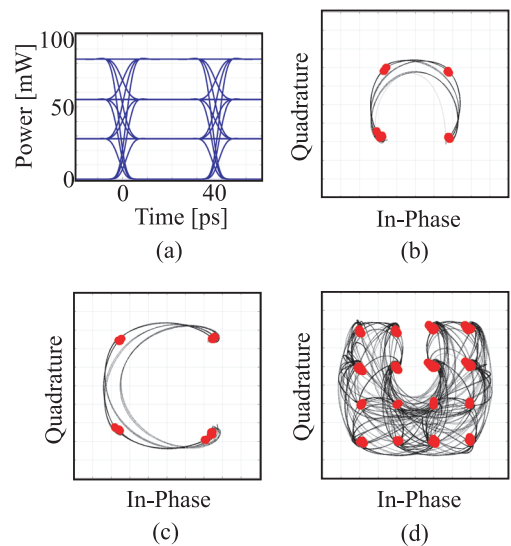

Fig. 3 Simulation model.

Table 2 Parameters of the HNLF @1550 nm.

Parameter	Value
Length [km]	2.5
Nonlinear coefficient [1/W/km]	13
Dispersion parameter [ps/nm/km]	0.57
Dispersion slope [ps/nm²/km]	−0.027
Loss [dB/km]	0.24

Fig. 4 (a) Eye diagram of the input PAM4 signal. Constellation diagrams of (b) QPSK 1, (c) QPSK 2, and (d) output 16QAM signals.
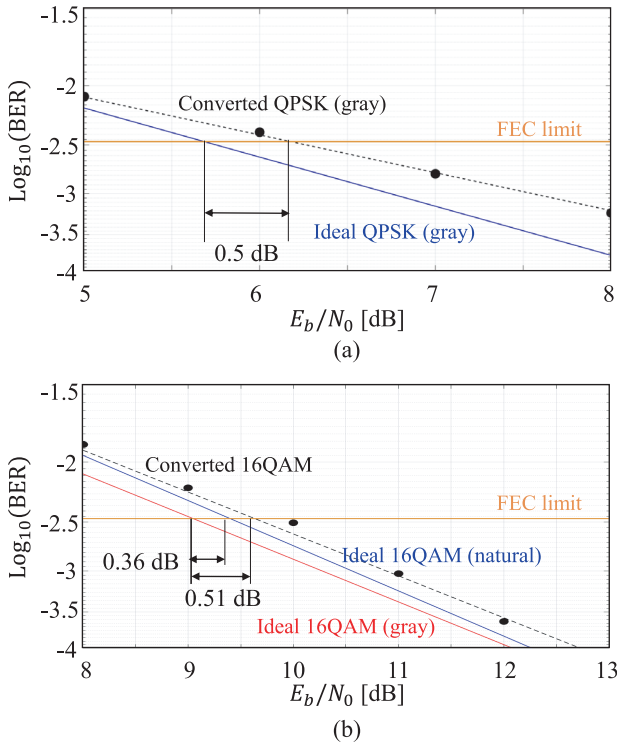
Fig. 5 BER curves of the converted (a) QPSK and (b) 16QAM signals.

Fig. 6 (a) Spectra of the converted 16QAM signal and the 16QAM signal generated by the ideal IQ modulator with Nyquist shaping. (b) Temporal waveforms of the converted QPSK signals 1 and 2.

Fig. 7 (a) EVM of the converted 16QAM with changing the pass bandwidth of the OBPF at port 4. Constellation diagrams when the pass bandwidth of the OBPF is (b) 0.3 nm, (c) 0.6 nm, and (d) 1 nm.

class 16QAM signal can be obtained, as shown in Fig. 4(d). The EVM of the converted 16QAM signal was 2.6%. This error is induced by a slight power variation of the probe light due to optical parametric amplification (OPA) caused by the interaction with the PAM4 pump lights. The power of the probe light, which depends on the peak power of the PAM4 signals, is amplified by a four-wave mixing process. Therefore, the converted QPSK signals exhibit slight power differences by the bit pattern of the PAM4 signal. This results in the degradation of the converted 16QAM signal.

Figure 5 shows the BER curves of the converted 16QAM signal. In this simulation, we assumed the use of a hard decision forward error correction (FEC) with the BER = 3.8×10^{-3} limit. A power penalty of 0.51 dB was observed for the converted 16QAM signal compared with the ideal 16QAM signal. This power penalty is caused by two effects: the OPA effect mentioned above and the restriction on the encoding. When we use gray-mapped PAM4 signals, the converted QPSK signals with gray coding can be obtained. However, the converted 16QAM signal obtained by coupling two QPSK signals is not gray coded.

Figure 6(a) shows the spectra of the converted 16QAM signal and the 16QAM signal generated by the ideal IQ modulator with Nyquist shaping. The converted 16QAM signal has a wider spectral width than that generated by the IQ modulator. This is due to the effect of frequency chirp during the conversion process. In this converter, the intensity of the PAM4 signal is transferred to the phase of the probe light. Thus, the phase of the probe light rapidly changes at the rise and fall timing edges of the PAM4 sig-
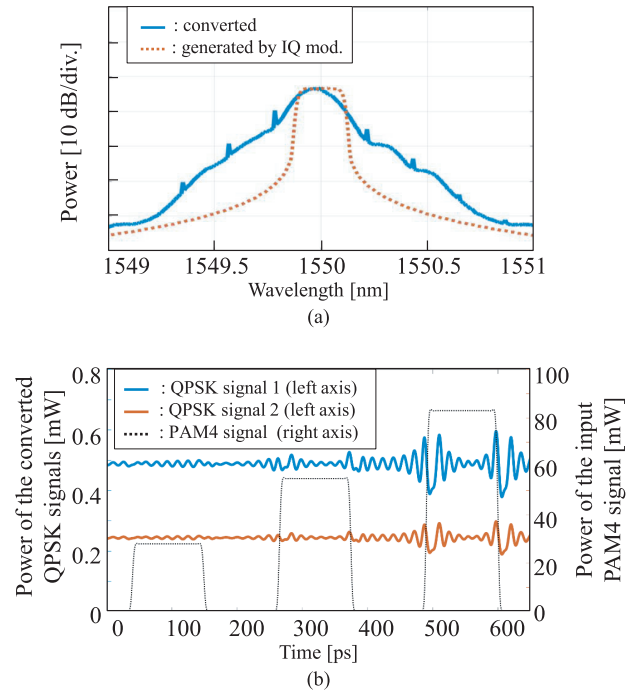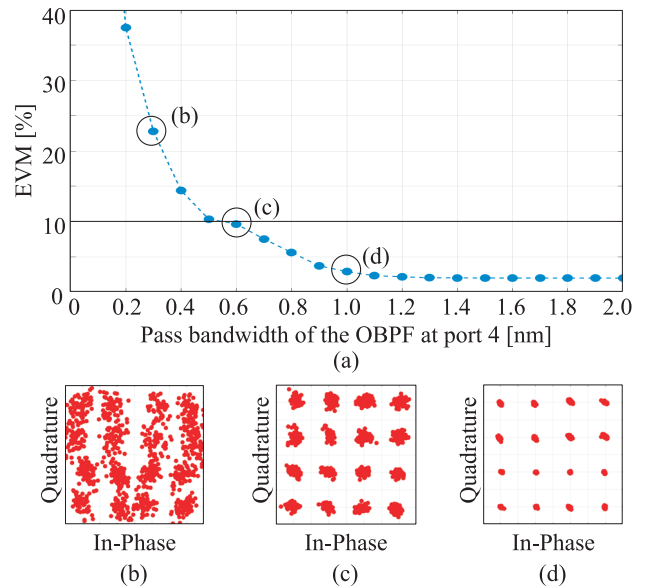
nals. Figure 6(b) shows the temporal waveforms of the converted QPSK signals 1 and 2. The intensity of the converted QPSK signals 1 and 2 fluctuates at the time of symbol transition because of the interaction between the frequency chirp and GVD effects in the HNLF.

Figure 7(a) shows the EVM of the converted 16QAM signal with changing the pass bandwidth of the OBPF at port
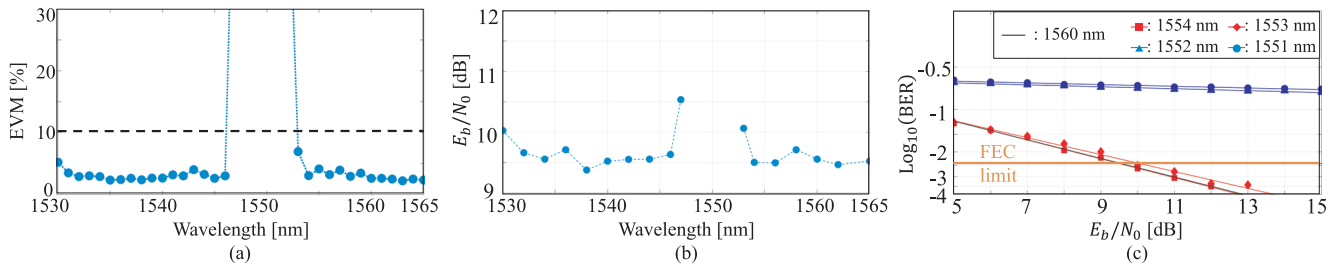
Fig. 8 (a) EVM, (b) E_b/N_0 to achieve FEC limit, (c) BER curves of the output 16QAM signal when the wavelength of PAM4 signal is changed.

4, and Fig. 7(b)–(d) shows the constellation diagrams when the pass bandwidth of the OBPF is 0.3 nm, 0.6 nm and 1 nm, respectively. When the pass bandwidth is 0.6 nm or more, the EVM can be kept lower than 10%. These results indicate that the converted 100 Gbps 16QAM signal is available by keeping a channel spacing of 0.6 nm in wavelength division multiplexing (WDM) inter-data center networks.

3.2 Influence of Input PAM4 Signal

In intra-data center networks, the wavelength of the PAM4 signal is different for each WDM channel. The power and timing of the PAM4 signal need to be properly adjusted for the conversion. This is because those after transmission are changed by channel and the transmitted path. Moreover, the waveform of the PAM4 signal is distorted by ASE noise of optical amplifier before the converter and chromatic dispersion effect through the intra-data center transmission. In this section, we show the conversion performance with changing the parameters of the input PAM4 signals (wavelength, power, input timing, and effects of ASE noise and dispersion).

3.2.1 Wavelength Dependence

Figure 8(a)–(c) show the the EVM, E_b/N_0 to achieve the FEC limit, and BER curves of the converted 16QAM signal with changing the wavelength of the PAM4 signal light in the C-band, respectively. The wavelength of the probe light was fixed to 1550 nm. The EVM and E_b/N_0 to achieve the FEC limit drastically increase when the wavelength of the PAM4 signal is close to the probe light wavelength of 1550 nm. This is because the probe light is amplified by the OPA. The OPA gain increases with the increase in pump light power of the PAM4 signal and decrease with the difference in wavelength between the PAM4 signal and probe light. The EVM can be kept below 10% at wavelength ranges of the input PAM4 signal of 1530–1547 and 1553–1565 nm in C-band. As shown in Fig. 8(b), the power penalty can be kept below 1 dB when the wavelength difference is 3 nm or more. The OPA causes a critical BER degradation when the wavelength deference is 2 nm or less. Note that it is difficult to convert from O-band PAM4 signal to C-band 16QAM signal due to walk-off effect in dispersive optical fiber. When we employ the proposed modulation for-

mat converter to connect data center networks, it is essential to combine it with wavelength converter.

3.2.2 Input Power Dynamic Range

We calculate the EVM to evaluate the tolerance of power deviation of the PAM4 signal in the proposed conversion. We consider a case that peak powers of the PAM4 signals 1 and 2 change independently. The peak power shifts $\Delta P_c^{(j)}$ and $\Delta P_{cc}^{(k)}$ from the ideal peak power $P_{c\_ideal}^{(j)}$ and $P_{cc\_ideal}^{(j)}$ of the PAM4 signals are defined as

$$\Delta P_c^{(j)} = P_c^{(j)} - P_{c\_ideal}^{(j)}, \quad (10)$$

$$\Delta P_{cc}^{(k)} = P_{cc}^{(k)} - P_{cc\_ideal}^{(k)}. \quad (11)$$

The phase shifts $\Delta\phi_c^{(j)}$ and $\Delta\phi_{cc}^{(k)}$ from ideal phase changes $\phi_{c\_ideal}^{(j)}$ and $\phi_{cc\_ideal}^{(k)}$ by XPM defined in Eqs. (3) and (5) are derived as

$$\Delta\phi_c^{(j)} = \phi_c^{(j)} - \phi_{c\_ideal}^{(j)} = 2\gamma L_{eff}\Delta P_c^{(j)}, \quad (12)$$

$$\Delta\phi_{cc}^{(k)} = \phi_{cc}^{(k)} - \phi_{cc\_ideal}^{(k)} = 2\gamma L_{eff}\Delta P_{cc}^{(k)}. \quad (13)$$

When a 16QAM signal is generated by coupling two QPSK signals, the EVM of the 16QAM signal is described as

$$\text{EVM} = \sqrt{2 - \frac{1}{40}\sum_{k=0}^{3}\sum_{j=0}^{3}b^{(j,k)}}, \quad (14)$$

where

$$
\begin{aligned}
b^{(j,k)} = {}& \cos\left(\Delta\phi_c^{(j)}\right) + 4\cos\left(\Delta\phi_{cc}^{(k)}\right) \\
& -2\cos\left(\phi_c^{(j)} - \phi_{cc\_ideal}^{(k)}\right) \\
& -2\cos\left(\phi_{c\_ideal}^{(j)} - \phi_{cc}^{(k)}\right) \\
& +2\cos\left(\phi_c^{(j)} - \phi_{cc}^{(k)}\right). \quad (15)
\end{aligned}
$$

Thus, when the average power of only the PAM4 signal 1 shifts from an ideal average power, the EVM of the converted 16QAM signal is described as

$$
\begin{aligned}
\text{EVM}_{\text{PAM4\_1}} &= \sqrt{2 - \frac{1}{40}\sum_{k=0}^{3}\sum_{j=0}^{3}\left(4 + \cos\left(\Delta\phi_c^{(j)}\right)\right)} \\
&= \sqrt{\frac{2}{5} - \frac{1}{10}\sum_{j=0}^{3}\cos\left(2\gamma L_{eff}\Delta P_c^{(j)}\right)}
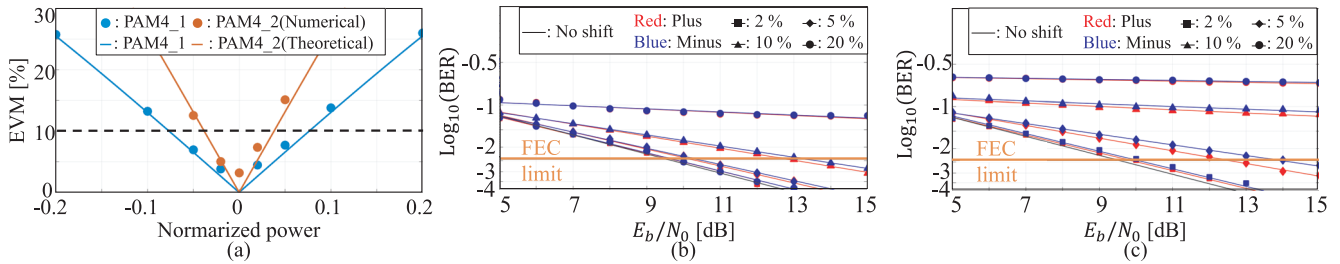\end{aligned}
$$

Fig. 9 (a) EVM, (b) BER curves (PAM4 signal 1), and (c) BER curves (PAM4 signal 2) of the output 16QAM signal when the power of the PAM4 signal is changed.
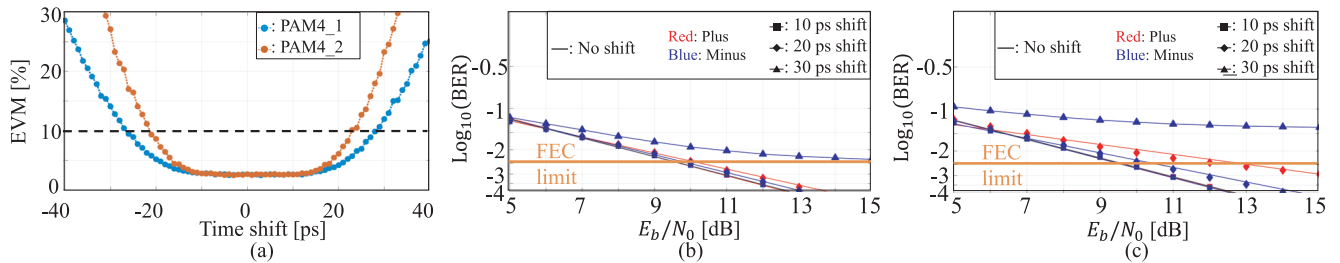

Fig. 10 (a) EVM, (b) BER curves (PAM4 signal 1), and (c) BER curves (PAM4 signal 2) of the output 16QAM signal when the input timing of the PAM4 signal is shifted.

$$= \sqrt{\frac{2}{5} - \frac{1}{10} \sum_{j=0}^{3} \cos\left(j \frac{\pi}{2} \frac{\overline{|\Delta P_{\mathrm{c}}|}}{\overline{P_{\mathrm{c\_ideal}}}}\right)}, \quad (16)$$

where $\overline{\Delta P_{\mathrm{c}}}/\overline{P_{\mathrm{c\_ideal}}}$ is the normalized average power shift of the PAM4 signal 1. In the same way,

$$\mathrm{EVM_{PAM4\_2}} = \sqrt{2 - \frac{1}{40} \sum_{k=0}^{3} \sum_{j=0}^{3} \left(1 + 4\cos\left(\Delta\phi_{\mathrm{cc}}^{(k)}\right)\right)}$$

$$= \sqrt{\frac{8}{5} - \frac{2}{5} \sum_{k=0}^{3} \cos\left(k \frac{\pi}{2} \frac{\overline{|\Delta P_{\mathrm{cc}}|}}{\overline{P_{\mathrm{cc\_ideal}}}}\right)}$$

$$= 2 \times \mathrm{EVM_{PAM4\_1}}, \quad (17)$$

where $\overline{\Delta P_{\mathrm{cc}}}/\overline{P_{\mathrm{cc\_ideal}}}$ is the normalized average power shift of the PAM4 signal 2. Considering the theoretical EVM values of the converted 16QAM signal, the power shift of the PAM4 signal 2 has a larger effect on the EVM than that of the PAM4 signal 1. This is because PAM4 signal 2 is converted to the QPSK signal 2, which has higher power than QPSK signal 1 in coupling. Figure 9(a) shows the EVM of the output 16QAM signal when the power of PAM4 signals 1 and 2 are changed by theory and numerical simulation. The theoretical EVM curves agree well with the numerical simulation results. The power shift of the PAM4 signal needs to be kept from −4% to +3% in the case of EVM ≤ 10%.

Figure 9(b) and (c) shows the BER characteristics of the output 16QAM signal when the power of the PAM4 signals 1 and 2 are changed, respectively. When the amount of the PAM4 signal 1 power shift is ±10%, the BER under the FEC limit can be achieved. On the other hand, serious BER

degradation occurs with the same amount of shift for the PAM4 signal 2. This trend is the same as the EVM degradation. The power of the PAM4 signal is the key parameter for the proposed conversion because the XPM effect in the HNLF is linearly dependent on the power of the PAM4 signal as described in Eqs. (3) and (5).

3.2.3 Tolerance of Input Timing

We evaluated the tolerance of the PAM4 signal input timing shift in the proposed conversion. Figure 10(a) shows the EVM of the output 16QAM signal when the input timings of PAM4 signals 1 and 2 are changed. Figure 10(b) and (c) shows the BER curves of the output 16QAM signal with changing the input timings of the PAM4 signals 1 and 2, respectively. As in the case of the power tolerance, PAM4 signal 2 has a larger effect on the timing tolerance than PAM4 signal 1. Both the EVM and BER of the converted 16QAM signal start to increase at an input timing shift of ±15~20 ps. The time slot of the 26.6-Gbaud PAM4 signal is about 38 ps, and the rise and fall times of the symbol transition are about 10 ps. Therefore, the stable time width of the peak power within the time slot is about 28 ps, which is almost the same value as the time range of a stable EVM. In other words, the allowable range of the input timing shift between two PAM4 signals is determined by the baud rate and rise/fall time of the PAM4 signals. In this simulation, the wavelength difference between the probe light and the PAM4 signal is 10 nm. In the case of a large difference in wavelengths, a walk-off effect degrades the tolerance of input timing. The input timing shift of the PAM4 signal needs to be kept ±20 ps in the case of EVM ≤ 10%.
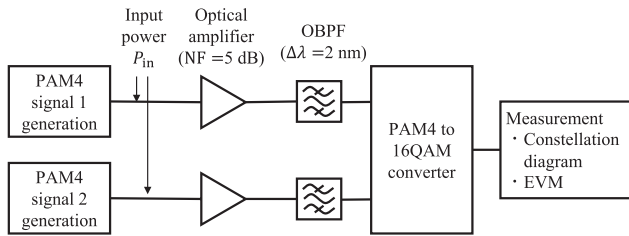
Fig. 11　Overview of the ASE noise simulation.
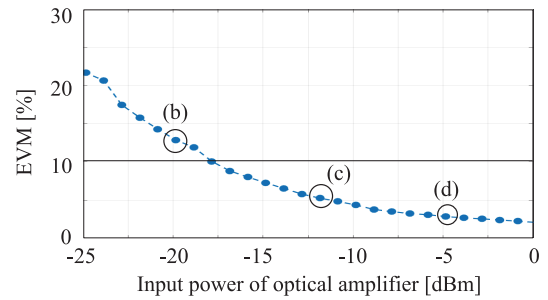

3.2.4　Effect of ASE Noise

In the proposed scheme, optical amplifiers are essential to amplify the PAM4 signals because high input powers of PAM4 signals are required. After the amplification, the PAM4 signals have waveform distortion due to ASE noise. An overview of the ASE noise simulation is shown in Fig. 11. The optical amplifiers were put before the proposed PAM4 to 16QAM converter. The ASE white noise power spectral density N_o at the output of the optical amplifier is described by [29]

$$N_o = h\nu n_{\mathrm{sp}}(G-1), \tag{18}$$

where n_{sp} is the spontaneous emission factor, G is the optical amplifier gain, h is Planck's constant, and ν is the optical frequency. n_{sp} has a relation of NF $\sim 2n_{\mathrm{sp}}$ with noise figure (NF). We investigated the effect of the ASE noise with changing input power P_{in} at the input of the optical amplifier. The power levels of the PAM4 signals at the output of the amplifier were maintained at 0, 28, 55, and 83 mW for the four signal levels. The NF of the optical amplifier was 5 dB and we assumed that the ASE noise followed a Gaussian distribution. The bandwidth of the OBPF after the optical amplifier was 2 nm.

　　Figure 12(a) shows the EVM of the converted 16QAM signal with changing the input power P_{in}. Figure 12(b)–(d) shows the eye diagrams of the distorted PAM4 signal and constellation diagrams of the converted 16QAM signal when the input powers were −20, −12 and −5 dBm, respectively. When the input power was low, the phase fluctuation of the converted 16QAM signal became larger. This is because that the power fluctuation of the PAM4 signal due to ASE noise is converted to the phase fluctuation of the converted 16QAM signal through XPM in HNLF. To be precise, the power fluctuations of the PAM4 signals are converted to the phase fluctuations of QPSK signals through XPM, subsequently the distorted 16QAM signal was generated by coupling two phase-distorted-QPSK signals. Therefore, some signal points of the converted 16QAM signal contained amplitude fluctuations. Figure 12(e) and (f) respectively shows the constellation diagrams when adding ASE noise to only the PAM4 signal 1 and only the PAM4 signal 2 (P_{in} = −12 dBm). The ASE noises of PAM4 signals 1 and 2 affected phase fluctuations of the small QPSK signal 1 and the large QPSK signal 2, respectively. Then,
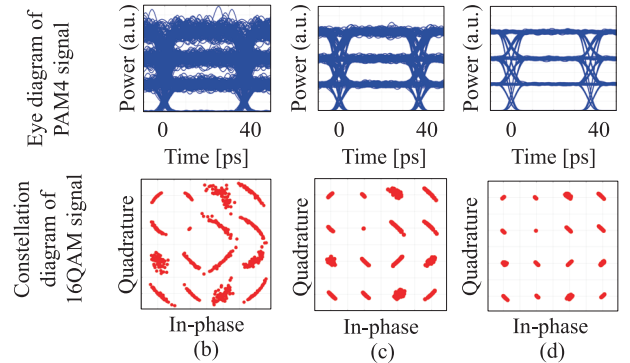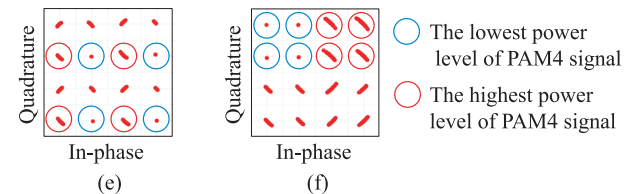
Fig. 12　Effect of ASE noise, (a) EVM of the converted 16QAM signal. (b)–(d) Eye diagrams of the PAM4 signal and constellation diagrams of the 16QAM signal when the input powers were −20, −12 and −5 dBm, respectively. Constellation diagrams when adding ASE noise to (e) only the PAM4 signal 1 and (f) only the PAM4 signal 2 (P_{in} = −12 dBm).

the higher power level of the PAM4 signal was, the larger the phase fluctuation was. This is because the phase change through XPM is proportional to the power level of PAM4 signal, that is square of the amplitude. The power fluctuation of the PAM4 signal was also large in the case of the high power level as shown in Fig. 12(b)–(d). Finally, the EVM of the converted 16QAM signal can be kept lower than 10% when the input power is −18 dBm or more. Assuming 400Gbase-LR-8 in IEEE802.3bs [4] with average launch power of transmitter of 0 dBm, fiber loss of 0.5 dB/km, and transmission distance of 10 km, the input power of the optical amplifier is −5 dBm. In this case, the well-defined constellation diagram of the converted 16QAM signal can be obtained as shown in Fig. 12(d).

　　Next, we analyzed the distribution of the phase noise of the converted 16QAM. Figure 13 shows histograms of phase of the representative signal points and fitting curves of Gaussian distribution based on maximum likelihood estimation when P_{in} = −23.8 dBm. As Fig. 13 indicates, the distribution of the phase noise of the converted 16QAM signal can be approximated by Gaussian distribution. This results
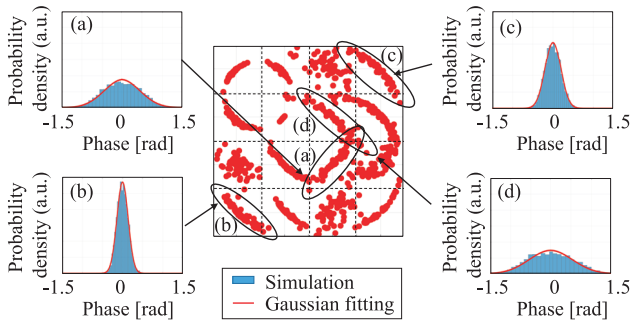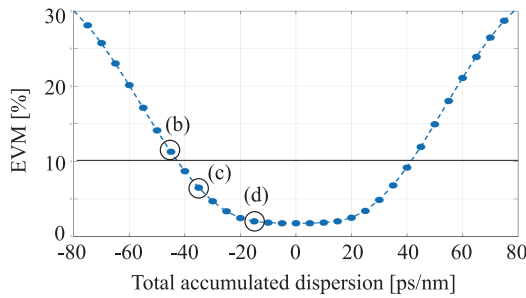
Fig. 13 Histograms of phase of the representative signal points and fitting curves of Gaussian distribution when $P_{in} = -23.8$ dBm.
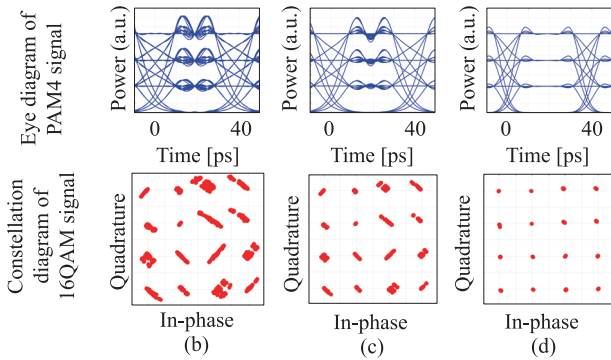

Fig. 14 Effect of chromatic dispersion, (a) EVM of the converted 16QAM signal. (b)–(d) Eye diagrams of the PAM4 signal and constellation diagrams of the 16QAM signal when the total accumulated dispersions were −45, −35 and −15 ps/nm.

are similar to the simulation results of the OOK/16QAM converter [10]. In typical optical fiber transmission system, nonlinear interference in WDM fiber channel can be also approximated by Gaussian-noise (GN) model [30]. Therefore, we can handle the phase noise of the converted 16QAM signal as an additional nonlinear phase noise in the typical digital coherent system.

3.2.5 Effect of Chromatic Dispersion

In intra-data center network of IEEE802.3bs [4], the PAM4 signals are transmitted through < 2 or < 10 km standard single mode fiber (SSMF). We investigated the effect of waveform distortion due to chromatic dispersion. Figure 14(a) shows the EVM of the converted 16QAM sig-

nal when the PAM4 signal is distorted by chromatic dispersion. Figure 14(b)–(d) shows the eye diagrams of the distorted PAM4 signal and constellation diagrams of the converted 16QAM signal when the total accumulated dispersions were −45, −35 and −15 ps/nm, respectively. The power fluctuation of the PAM4 signal due to dispersion effect is converted to the phase fluctuation of the 16QAM signal as well as the case of ASE noise effect. The EVM of the converted 16QAM signal can be kept lower than 10% when the total accumulate dispersion is from −42 to +42 ps/nm. In IEEE802.3bs, 8 WDM channels of wavelength from 1273.55 to 1309.14 nm are adopted. Assuming SSMF with zero dispersion wavelength of 1300 nm and dispersion slope of 0.092 ps/nm^2/km [31], the range of dispersion parameter is from −2.4 to 0.8 ps/nm/km (1273.55–1309.14 nm). In this case, 2 and 10 km transmissions of 400Gbase-FR-8 and 400Gbase-ER-8 are acceptable because the range of the accumulated dispersion is from −24 to 8 ps/nm with the 10 km transmission. For future intra-data center network of higher baud rate and longer transmission distance, high dispersion tolerant schemes are still open for discussion, such as precompensation of PAM4 signal and additional all-optical approach including combination with dispersion compensation or signal regeneration.

4. Conclusions

In this paper, we proposed a novel all-optical modulation format conversion from PAM4 to 16QAM using NOLM and a 1:2 coupler. The successful operation of the conversion from 2×26.6-Gbaud PAM4 signals to a 100-Gbps class 16QAM signal was demonstrated by numerical simulation. Compared with an ideal 16QAM signal, the power penalty of the converted 16 QAM signal could be kept within 0.5 dB. The spectrum of the converted 16QAM signal is wider than that of an ideal 16QAM signal. However, the converted 100 Gbps 16QAM signal is available by keeping a WDM channel spacing of 0.6 nm in inter-data center networks. Furthermore, we discussed the conversion performance of the wavelength, input power, and input timing dependence of the PAM4 signal. Then, we demonstrated effects of the waveform distortion of the PAM4 signal due to ASE noise and chromatic dispersion.

References

[1] Cisco Systems, Inc., "Cisco visual networking index: Forecast and trends, 2017–2022," Feb. 2019.

[2] E. Yamazaki, S. Yamanaka, Y. Kisaka, T. Nakagawa, K. Murata, E. Yoshida, T. Sakano, M. Tomizawa, Y. Miyamoto, S. Matsuoka,

J. Matsui, A. Shibayama, J. Abe, Y. Nakamura, H. Noguchi, K. Fukuchi, H. Onaka, K. Fukumitsu, K. Komaki, O. Takeuchi, Y. Sakamoto, H. Nakashima, T. Mizuochi, K. Kubo, Y. Miyata, H. Nishimoto, S. Hirano, and K. Onohara, "Fast optical channel recovery in field demonstration of 100-Gbit/s Ethernet over OTN using real-time DSP," OSA Opt. Express, vol.19, no.14, pp.13179–13184, June 2007.

[3] H. Maeda, T. Kotanigawa, K. Saito, M. Yokota, S. Yamamoto, M. Suzuki, and T. Seki, "Field trial of simultaneous 100-Gbps and 400-Gbps transmission using advanced digital coherent technologies," Proc. Opt. Fiber Commun. Conf. (OFC2016), Paper W1K.4, Anaheim, US, March 2016.

[4] IEEE P802.3bs/D3.4, Draft standard for ethernet amendment: Media access control parameters, physical layers and management parameters for 200 Gb/s and 400 Gb/s, Oct. 2017.

[5] A.E. Willner, A. Fallahpour, F. Alishahi, Y. Cao, A.M.-Ariaei, A. Almaiman, P. Liao, K. Zou, A.N. Willner, and M. Tur, "All-optical signal processing techniques for flexible networks," IEEE/OSA J. Lightw. Technol., vol.37, no.1, pp.21–35, Jan. 2019.

[6] K. Mishina, D. Hisano, and A. Maruta, "All-optical modulation format conversion and applications in future photonic networks," IEICE Trans. Electron., vol.E102-C, no.4, pp.304–315, April 2019.

[7] K. Mishina, A. Maruta, S. Mitani, T. Miyahara, K. Ishida, K. Shimizu, T. Hatta, K. Motoshima, and K. Kitayama, "NRZ-OOK to RZ-BPSK modulation-format conversion using SOA-MZI wavelength converter," IEEE/OSA J. Lightw. Technol., vol.24, no.10, pp.3751–3758, Oct. 2006.

[8] K. Mishina, S. Kitagawa, and A. Maruta, "All-optical modulation format conversion from on-off keying to multiple-level phase-shift-keying based on nonlinearity in optical fiber," OSA Opt. Express, vol.15, no.13, pp.8444–8453, June 2007.

[9] K. Mishina, S.M. Nissanka, A. Maruta, S. Mitani, K. Ishida, K. Shimizu, T. Hatta, and K. Kitayama, "All-optical modulation format conversion from NRZ-OOK to RZ-QPSK using parallel SOA-MZI OOK/BPSK converters," OSA Opt. Express, vol.15, no.12, pp.7774–7785, June 2007.

[10] G. Huang, Y. Miyoshi, A. Maruta, and K. Kitayama, "All-optical technique for modulation format conversion from NRZ-OOK to RZ-16QAM employing nonlinear optical loop mirror with 1 : 2 coupler," OSA Opt. Express, vol.20, no.24, pp.27311–27321, Nov. 2012.

[11] T. Kodama, T. Miyazaki, and M. Hanawa, "Seamless PAM-4 to QPSK modulation format conversion at gateway for short-reach and long-haul integrated networks," Proc. 44th European Conf. on Opt. Commun. (ECOC2018), Paper We3H, Roma, Italy, Sept. 2018.

[12] A.-L. Zhang and M.-C. Yang, "Tunable modulation format conversion based on spectral line-by-line pulse shaper for all-optical signal processing," Springer Optoelectron. Lett., vol.10, pp.228–231, May 2014.

[13] H. Kishikawa, P. Seddighian, N. Goto, S. Yanagiya, and R.L. Chen, "All-optical modulation format conversion from binary to quadrature phase-shift keying using delay line interferometer," Proc. IEEE Photon. Conf. (IPC2011), Paper WO2, Arlington, US, Sept. 2011.

[14] F. Parmigiani, L. Jones, J. Kakande, P. Petropoulos, and D.J. Richardson, "Modulation format conversion employing coherent optical superposition," OSA Opt. Express, vol.20, no.26, pp.B322–B330, Nov. 2012.

[15] A. Fallahpour, A. Mohajerin-Ariaei, A. Almaiman, Y. Cao, F. Alishahi, C. Bao, P. Liao, M. Ziyadi, B. Shamee, D. Starodubov, M. Tur, C. Langrock, M.M. Fejer, J. Touch, and A.E. Willner, "Demonstration of 30 Gbit/s QPSK-to-PAM4 data-format and wavelength conversion to enable all-optical gateway from long-haul to data center," Proc. Opt. Fiber Commun. Conf. (OFC2018), Paper W2A.22, San Diego, US, March 2018.

[16] F. Da Ros, K. Dalgaard, L. Lei, J. Xu, and C. Peucheret, "QPSK-to-2×BPSK wavelength and modulation format conversion through phase-sensitive four-wave mixing in a highly nonlinear optical fiber," OSA Opt. Express, vol.21, no.23, pp.28743–28750, Nov. 2013.

[17] F.D. Ros, K. Dalgaard, Y. Fukuchi, J. Xu, M. Galili, and C. Peucheret, "Simultaneous QPSK-to-2×BPSK wavelength and modulation format conversion in PPLN," IEEE/OSA Photon. Technol. Lett., vol.26, no.12, pp.1207–1210, April 2014.

[18] K. Mori, H. Kishikawa, and N. Goto, "Time and wavelength dependency on QPSK to 16QAM modulation format conversion using delay line interferometer," Proc. Third International Forum on Advanced Technol. (IFAT2017), Paper FS17, Taroko, Taiwan, March 2017.

[19] A. Fallahpour, M. Ziyadi, A. Mohajerin-Ariaei, Y. Cao, A. Almaiman, F. Alishahi, C. Bao, P. Liao, B. Shamee, L. Paraschis, M. Tur, C. Langrock, M.M. Fejer, J. Touch, and A.E. Willner, "Experimental demonstration of tunable optical de-aggregation of each of multiple wavelength 16-QAM channels into two 4-PAM channels," Proc. Opt. Fiber Commun. Conf. (OFC2017), Paper Th4I.6, Los Angeles, US, March 2017.

[20] A. Bogris, "All-optical demultiplexing of 16-QAM signals into QPSK tributaries using four-level optical phase quantizers," OSA Opt. Lett., vol.39, no.7, pp.1775–1778, April 2014.

[21] T. Kato, S. Watanabe, T. Tanimura, T. Richter, R. Elschner, C. Schmidt-Langhorst, C. Schubert, and T. Hoshida, "THz-range optical frequency shifter for dual polarization WDM signals using frequency conversion in fiber," IEEE/OSA J. Lightw. Technol., vol.35, no.6, pp.1267–1273, Oct. 2018.

[22] J. Leuthold, L. Moller, J. Jaques, S. Cabot, L. Zhang, P. Bernasconi, M. Cappuzzo, L. Gomez, E. Laskowski, E. Chen, A. Wong-Foy, and A. Griffin, "160 Gbit/s SOA all-optical wavelength converter and assessment of its regenerative properties," IEEE Electron. Lett., vol.40, no.9 pp.554–555, April 2004.

[23] M.A. Foster, A.C. Turner, R. Salem, M. Lipson, and A.L. Gaeta, "Broad-band continuous-wave parametric wavelength conversion in silicon nanowaveguides," OSA Opt. Express, vol.15, no.20, pp.12949–12958, Oct. 2007.

[24] C. Langrock, S. Kumar, J.E. McGeehan, A.E. Willner, and M.M. Fejer, "All-optical signal processing using χ^2 nonlinearities in guided-wave devices," IEEE/OSA J. Lightw. Technol., vol.24, no.7, pp.2579–2592, July 2006.

[25] D. Kong, M. Pu, Y. Liu, Y. Zheng, E. Semenova, K. Yvind, L.K. Oxenlowe, M. Galili, and H. Hu, "744-nm wavelength conversion of PAM-4 signal using an AlGaAsOI nanowaveguide," OSA Opt. Lett., vol.45, no.4, pp.889–892, Feb. 2020.

[26] N. Ophir, R.K.W. Lau, M. Ménard, R. Salem, K. Padmaraju, Y. Okawachi, M. Lipson, A.L. Gaeta, and K. Bergman, "First demonstration of a 10-Gb/s RZ end-to-end four-wave-mixing based link at 1884 nm using silicon nanowaveguides," IEEE/OSA Photon. Technol. Lett., vol.24, no.4, pp.276–278, Feb. 2012.

[27] S. Punhavan, M. Kato, K. Sugiyama, M. Asobe, T. Umeki, K. Enbutsu, T. Kazama, T. Kashiwazaki, and R. Kasahara, "1.4 μm–1.6 μm wavelength conversion using multiple quasi-phase matching LiNbO3," Proc. 24th OptoElectronics and Commun. Conf. International Conf. on Photon. in Switching and Computing 2019 (OECC/PSC 2019), Paper WB3-2, July 2019.

[28] G.P. Agrawal, Nonlinear Fiber Optics, 5th ed., Academic Press, Cambridge, MA, 2012.

[29] S. Bottacchi, Noise and Signal Interference in Optical Fiber Transmission Systems, Wiley, Chichester, UK, 2008.

[30] P. Poggiolini, G. Bosco, A. Carena, V. Curri, Y. Jiang, and F. Forghieri, "The GN-Model of fiber non-linear propagation and its applications," IEEE/OSA J. Lightw. Technol., vol.32, no.4, pp.694–721, Oct. 2014.

[31] ITU-T, G.652, "Characteristics of a single-mode optical fibre and cable," Nov. 2016.

Yuta Matsumoto received the B.E. degree in electrical, electronic and information engineering from Osaka University, Osaka, Japan, in 2019. He is currently working toward the M.E. degree at Osaka University. Mr. Matsumoto is a Student Member of the Institute of Electronics, Information, and Communication Engineers of Japan.

Ken Mishina received the B.E., M.E., and Ph.D. degrees in electrical, electronic, and information engineering from Osaka University, Osaka, Japan, in 2005, 2007, and 2012, respectively. In 2007, he joined Shimadzu Corporation, Kyoto, Japan. Since 2018, he has been an Associate Professor with the Department of Information and Communication Technology, the Division of Electrical, Electronic, and Information Engineering, Graduate School of Engineering, Osaka University. His current research interests include optical fiber communication systems, all-optical signal processing and photovoltaics. Dr. Mishina is a member of the IEEE Photonics Society and the Institute of Electronics, Information, and Communication Engineers (IEICE) of Japan.

Daisuke Hisano received the B.E., M.E., and Ph.D. degrees in electrical, electronic and information engineering from Osaka University, Osaka, Japan, in 2012, 2014, and 2018, respectively. In 2014, he joined NTT Access Network Service Systems Laboratories, Yokosuka, Japan. Since 2018, he has been an Assistant Professor with the Department of Information and Communication Technology, the Division of Electrical, Electronic, and Information Engineering, Graduate School of Engineering, Osaka University. His research interests include optical-wireless converged networks, optical communication, and all-optical signal processing. He is a member of the IEEE and the IEICE of Japan.

Akihiro Maruta received the B.E., M.E., and Ph.D. degrees from Osaka University, Osaka, Japan, in 1988, 1990, and 1993, respectively, all in communications engineering. He was with the Department of Communications Engineering, Osaka University, in 1993. He has been a Professor in the Department of Information and Communication Technology, Osaka University, since 2016. His current research interests include optical fiber communication systems and all-optical signal processing. Dr. Maruta is a member of the IEEE Photonics Society and the Optical Society of America, and a senior member of the IEICE.